

THE PAN-PACIFIC PLANET SEARCH VI: GIANT PLANETS ORBITING HD 86950 AND HD 222076

ROBERT A. WITTENMYER^{1,2}, M.I. JONES³, JINGLIN ZHAO², J.P. MARSHALL², R.P. BUTLER⁴, C.G. TINNEY², LIANG WANG⁵,
JOHN ASHER JOHNSON⁶

¹Computational Engineering and Science Research Centre, University of Southern Queensland, Toowoomba, Queensland 4350, Australia

²School of Physics and Australian Centre for Astrobiology, UNSW Australia, Sydney 2052, Australia

³Department of Electrical Engineering and Center of Astro-Engineering UC, Pontificia Universidad Católica de Chile, Av. Vicuña Mackenna 4860, 782-0436 Macul, Santiago, Chile

⁴Department of Terrestrial Magnetism, Carnegie Institution of Washington, 5241 Broad Branch Road, NW, Washington, DC 20015-1305, USA

⁵Key Laboratory of Optical Astronomy, National Astronomical Observatories, Chinese Academy of Sciences, A20 Datun Road, Chaoyang District, Beijing 100012, China

⁶Harvard-Smithsonian Center for Astrophysics, Cambridge, MA 02138 USA

ABSTRACT

We report the detection of two new planets orbiting the K giants HD 86950 and HD 222076, based on precise radial velocities obtained with three instruments: AAT/UCLES, FEROS, and CHIRON. HD 86950b has a period of 1270 ± 57 days at $a = 2.72 \pm 0.08$ AU, and $m \sin i = 3.6 \pm 0.7 M_{\text{Jup}}$. HD 222076b has $P = 871 \pm 19$ days at $a = 1.83 \pm 0.03$ AU, and $m \sin i = 1.56 \pm 0.11 M_{\text{Jup}}$. These two giant planets are typical of the population of planets known to orbit evolved stars. In addition, we find a high-amplitude periodic velocity signal ($K \sim 50 \text{ m s}^{-1}$) in HD 29399, and show that it is due to stellar variability rather than Keplerian reflex motion. We also investigate the relation between planet occurrence and host-star metallicity for the 164-star Pan-Pacific Planet Search sample of evolved stars. In spite of the small sample of PPPS detections, we confirm the trend of increasing planet occurrence as a function of metallicity found by other studies of planets orbiting evolved stars.

Keywords: planetary systems, stars: giants, stars: individual (HD 29399, HD 86950, HD 222076), techniques: radial velocity

1. INTRODUCTION

Nearly all our knowledge of planets orbiting stars more massive than the Sun comes from Doppler surveys targeting these stars after they have evolved off the main sequence. Subgiants and first-ascent giants are suitable radial velocity targets because their surface gravities remain high enough ($\log g \gtrsim 3$) to avoid the large-amplitude pulsations common in red giants (Hekker et al. 2008). Many groups have been conducting precise radial velocity surveys of these stars, with ~ 1000 total targets and 10-15 years of observations (e.g. Sato et al. 2005; Johnson et al. 2006; Reffert et al. 2015).

The Pan-Pacific Planet Search (PPPS - Wittenmyer et al. 2011b) operated on the 3.9m Anglo-Australian Telescope (AAT) between 2009 and 2015, surveying 164 southern giant stars in search of planets as a southern extension of the Northern “retired A stars” programme (Johnson et al. 2006). Since the conclusion of AAT observations in 2014, we have published a series of planet discoveries combining PPPS observations with data from the Okayama planet search (Sato et al. 2013, 2016) and the Chile-based EXPRESS survey, with which we share 37 targets (Wittenmyer et al. 2015, 2016a,b; Jones et al. 2016).

We have secured enough detections from the PPPS sample to make quantitative statements about the occurrence rate of giant planets orbiting evolved stars. For dwarf stars, the metallicity [Fe/H] is now well-known to be positively correlated with the probability of hosting a giant planet (e.g. Gonzalez 1997; Santos et al. 2001; Fischer & Valenti 2005). This is a consequence of the core-accretion model of planet formation, wherein metal-rich disks are more efficient at forming cores due to their enhanced surface density of solids (Pollack et al. 1996).

For giant stars, however, there remains disagreement as to the presence of such a planet-metallicity correlation.

Hekker & Meléndez (2007) found that planet-hosting giants had metallicities 0.13 ± 0.03 dex higher than the overall sample of 380 G and K giants. Their conclusion was bolstered by a subsequent analysis of the same sample with a further seven years of observational data (Reffert et al. 2015). But Takeda et al. (2008) found no difference in the metallicities of planet hosts versus non-hosts in their 322-star Okayama Planet Search sample. A preliminary analysis of the Penn State-Torun Planet Search sample by Zieliński et al. (2010) hinted at an anticorrelation, with the metallicities of RV-variable giant stars 0.15 ± 0.06 dex lower than the RV-stable stars. Maldonado et al. (2013) and Mortier et al. (2013) analysed large samples of giant stars, derived stellar parameters in a homogeneous manner, and found no significant metallicity differences between stars hosting planets and those not. More recently, however, Jones et al. (2016) presented an analysis of 166 giant stars and found a distinct peak in planet occurrence at $[\text{Fe}/\text{H}] \sim +0.35$. Clearly, the issue is far from settled.

In this paper, we present two new giant planets from the PPPS sample, in conjunction with data from the EXPRESS survey (Jones et al. 2011). Section 2 briefly describes the observational data and host star properties. Section 3 gives the results of the orbit fitting and describes the vetting process, and Section 4 places these planetary systems in context and discusses the planet-metallicity correlation within the PPPS sample.

2. OBSERVATIONS AND STELLAR PROPERTIES

Observations have been obtained with three instruments in two parallel planet-search efforts using the UCLES spectrograph (Diego et al. 1990) on the AAT, the CHIRON spectrograph (Tokovinin et al. 2013) on the 1.5m telescope at CTIO, and the FEROS spectrograph on the on the 2.2m telescope at La Silla (Kaufer et al. 1999).

UCLES delivers a resolution of $\lambda/\Delta\lambda \approx 45,000$ with a 1 arcsecond slit, on which an iodine cell imprints a dense forest of narrow absorption lines used to calibrate the instrumental point-spread function is calibrated (Valenti et al. 1995; Butler et al. 1996). FEROS on the 2.2m telescope at La Silla has a resolving power of $\sim 48,000$, and uses a ThArNe lamp for precise wavelength calibration. The instrument is equipped with a simultaneous calibration fibre which is used to correct the night spectral drift. The FEROS radial velocities were computed using the simultaneous calibration method (Baranne et al. 1996), using an improved reduction code presented in Jones et al. (2016; submitted). CHIRON is fed by a single fibre and an image slicer, delivering high resolution ($R \sim 80,000$) and higher efficiency than the slit and narrow slit modes, also available. The CHIRON echelle spectra are comprised of 71 orders covering a wavelength range between ~ 4100 - 8800 Å. The spectrograph is also equipped with an iodine cell, which superimposes a rich absorption spectrum in 22 different orders covering between ~ 5000 - 6200 Å. The radial velocities are computed with the iodine cell technique (Butler et al. 1996), following the newest reduction code described in Jones et al. (2016; submitted). A summary of the observations is given in Table 1, and the velocities from UCLES, FEROS, and CHIRON are given in Tables 2-4.

Stellar properties were derived from iodine-free template UCLES spectra with $R \sim 60,000$ as described fully in Wittenmyer et al. (2016d). In brief, spectroscopic stellar parameters were determined via a standard 1D, local thermodynamic equilibrium (LTE) abundance analysis using the 2013 version of MOOG (Snedden 1973) with the ODFNEW grid of Kurucz ATLAS9 model atmospheres (Castelli & Kurucz 2003). Complete stellar parameters from Wittenmyer et al. (2016d) and other literature sources are given in Table 5.

3. ORBIT FITTING AND COMPANION PARAMETERS

Although the data for these stars are sparse and poorly sampled, inspection suggested the presence of velocity signals, belied by the higher than usual scatter. Following a well-trodden path (e.g. Tinney et al. 2011; Wittenmyer et al. 2015, 2016a), we first used a genetic algorithm to search a wide range of orbital periods, running for 10,000 iterations (about 10^6 possible configurations). The period ranges were chosen based on visual inspection of the velocity data and are as follows: HD 29399 – [700-1100d]; HD 86950 – [1100-1400d]; HD 222076 – [800-1100d]. In all cases, convergence occurred rapidly, a hallmark of a genuine signal. Again as in our previous work, we then used the best solution from the genetic algorithm as a starting point for fitting with a Keplerian model in the *Systemic Console* version 2.1730 (Meschiari et al. 2009). For all orbit fitting, 7 m s^{-1} of jitter has been added in quadrature to the internal instrumental uncertainties of each data set. This estimate is derived from the velocity scatter of 37 stable stars in the PPPS as first described in Wittenmyer et al. (2016b). Finally, we estimated the parameter uncertainties using the bootstrap routine within *Systemic* on 10,000 synthetic data set realisations. The results are given in Table 6.

3.1. HD 29399: A false positive

We find that the velocities for HD 29399 can be fit with a planet having $P = 765 \pm 15$ days and $K = 52 \pm 34 \text{ m s}^{-1}$; the large uncertainty can be attributed to phase gaps which allow for a family of high-eccentricity solutions. As in our

previous work, we checked the All-Sky Automated Survey (ASAS) V band photometric data (Pojmanski & Maciejewski 2004) for variability due to intrinsic stellar processes. We analysed a total of 984 epochs spanning 8.36 years, with a mean value of 6.07 ± 0.32 mag. This scatter is an order of magnitude larger than that found for previously confirmed planet hosts from the PPPS (Wittenmyer et al. 2015, 2016b). The generalised Lomb-Scargle periodogram of this photometry (Zechmeister & Kürster 2009) is shown in Figure 1, with the period of the candidate planet marked as a vertical dashed line. There is an extremely significant periodicity squarely at the ~ 765 day period of our radial velocities. Given this evidence and the large photometric variability, we must conclude that the $K \sim 50 \text{ m s}^{-1}$ signal in the radial velocities is intrinsic to the star and not due to an orbiting planet. While stellar rotation is frequently the culprit in radial velocity false positives (e.g. Robertson et al. 2015; Rajpaul et al. 2016; Johnson et al. 2016), it is extremely unlikely in the case of HD 29399. The projected rotational velocity determined by De Medeiros et al. (2014) is less than 1.2 km s^{-1} ; using the stellar radius of $4 R_{\odot}$ in Table 5, this gives a rotation period of 169 days. Of course, since the measured $v \sin i$ is a lower bound, it remains possible that the true rotational velocity is smaller, arising from a nearly pole-on orientation. However, such an orientation would require an unreasonably high spot coverage to produce the observed variations in the radial velocities. In Section 4.1, we note that HD 29399 may host a debris disk; one might imagine quasi-periodic transits by debris (e.g. Vanderburg et al. 2015; Croll et al. 2015; Rappaport et al. 2016) to cause the photometric and radial velocity variations much as starspots would. However, we show in Section 4.1 that the required debris is best modelled at 1500K, and hence must orbit far too close to the star to produce a 765-day period by Keplerian orbital motion. Indeed, for such a long periodicity, the most likely source is a stellar magnetic activity cycle. In Section 3.3, we give further evidence via an analysis of the $H\alpha$ feature.

3.2. Single planets orbiting HD 86950 and HD 222076

For HD 86950, we find a clear signal with $P = 1270 \pm 57$ days and $K = 49 \pm 12 \text{ m s}^{-1}$, corresponding to a planet with $m \sin i$ of $3.6 \pm 0.7 M_{\text{Jup}}$ adopting a host star mass of $1.66 M_{\odot}$. The data and model fit are shown in Figure 2. Examination of 8.9 years (515 epochs) of ASAS photometry shows no periodicities of significance near the planet’s orbital period (Figure 3). The ASAS V band photometry has a mean value of 7.47 ± 0.02 mag.

For HD 222076, all three instruments clearly reveal a planet with $P = 871 \pm 19$ days and $m \sin i = 1.56 \pm 0.11 M_{\text{Jup}}$ assuming a host star mass of $1.07 M_{\odot}$ (Wittenmyer et al. 2016d). The orbit is nearly circular, and this fit has residuals of 5.9 m s^{-1} (Figure 4). Again, the ASAS photometry reveals no significant periodicities near the planet’s orbital period (Figure 5). The ASAS V band photometry has a mean value of 7.46 ± 0.02 mag. For this star, we have 5.67 years of FEROS spectra, uncontaminated by iodine, from which we can derive several activity indices (bisector velocity span, CCF FWHM, and S-index). None of these indicators (Table 4.2) show any periodicities or correlations with the radial velocities. We are thus confident that the observed velocity variations are due to an orbiting planet.

3.3. H -alpha activity index

In light of recent debate over the detection of planet-induced stellar reflex motion amidst the confounding effect of stellar activity (e.g. Robertson et al. 2014; Anglada-Escudé & Tuomi 2015; Fischer et al. 2016), we discuss in this section the $H\alpha$ activity indices for the three stars considered here.

Stellar activity can induce spurious velocity signatures that mimic the velocities produced by exoplanets. This can appear at the stellar rotation period or its harmonics (Boisse et al. 2011). Magnetic cycles can also produce radial velocity signals comparable in amplitude to orbiting planets (e.g. Santos et al. 2010; Dumusque et al. 2011; Robertson et al. 2015; Faria et al. 2016). Multiple mechanisms can produce these line profile variations. For example, variable levels of chromospheric activity can produce changes in the level of line profile reversal in some line cores, resulting in changes to both the line centroid and hence the measured radial velocity (Martínez-Arnáiz et al. 2010). These effects will also produce changes in the line’s equivalent width (EW), and so measurement of the EW can provide an indicator of the presence of activity-induced radial velocity variations (Robertson et al. 2014). Stellar activity is also seen to be correlated with the presence of starspots (Berdyugina 2005; Strassmeier 2009; Davenport 2015) and suppression of convection (Haywood et al. 2016), which will produce changes in line profile shapes and so line centroids, resulting in velocity jitter (Reiners et al. 2010; Andersen & Korhonen 2015). So EW measurements for a line-profile sensitive feature would be expected to be correlated with this source of jitter as well.

We have therefore measured the equivalent width of $H\alpha$ absorption as an indicator of variability in chromospheric activity. Our analysis builds on that presented by (Robertson et al. 2014), with the addition of an automated algorithm for continuum normalisation and telluric contamination identification in the region of the $H\alpha$ line. This method (detailed in the Appendix) has the advantage of being robust for arbitrary, slowly varying continua selection, without being parametric for the specific shape of the continuum or the location of specific absorption lines.

We show the stacked spectra of the three stars featured in this work, along with their RV-EW relations (Fig. 6–8). For HD 29399, where a strong ~ 2 -year periodicity was evident in the photometry and the radial velocities, we find a correlation between the $H\alpha$ equivalent width and the radial velocity, further evidence that the RV periodicity is intrinsic to the star and is most likely the result of a magnetic activity cycle as noted in Section 3.1. For the candidate planet hosts HD 86950 and HD 222076, no correlations are seen from the RV-EW plots, supporting our claim that the detected RV variations are not due to chromospheric stellar activity.

4. DISCUSSION AND CONCLUSIONS

HD 86950b and HD 222076b are typical of the population of planets being found to orbit evolved stars, which are generally beyond 1 AU and with masses greater than $1 M_{\text{Jup}}$ (e.g. Lovis & Mayor 2007; Döllinger et al. 2009; Bowler et al. 2010; Jones et al. 2014). Figure 9 places these two planets in context with the other planets known to orbit giant stars (i.e. stars with $\log g < 3.5$). Of the 107 such planets confirmed¹, the median semimajor axis is 1.38 AU, and the median $m \sin i$ is $1.38 M_{\text{Jup}}$.

4.1. Possible debris discs

HD 86950 has been identified by McDonald et al. (2012) as having a possible infrared excess based on the presence of excess emission at $9 \mu\text{m}$ in the AKARI/IRC All-Sky Survey (Ishihara et al. 2010), with a fractional luminosity ($L_{\text{dust}}/L_{\text{star}}$) of $\sim 1.2 \times 10^{-3}$. The presence of both a planetary system *and* a debris disc around HD 86950 would make it a nearly-unique object amongst sub-giant stars, joining κ CrB (HD 142091) as one of very few examples of an evolved star hosting both a debris disc and exoplanet Bonsor et al. (2013). Confirmation of this excess (and a better determination of the disc’s properties if confirmed) is therefore critical.

We compiled a spectral energy distribution from photometry spanning optical to mid-infrared wavelengths, including optical BV , near-infrared 2MASS JHK_s (Skrutskie et al. 2006), and mid-infrared MSX (Egan et al. 2003) and WISE (Wright et al. 2010) measurements, in addition to the AKARI $9 \mu\text{m}$ datum. We fit the stellar photospheric emission with a model from the BT-SETTL/Nextgen stellar atmospheres grid appropriate for the spectral type (K0III; $T_{\text{eff}} = 4750$ K, $\log g = 2.0$, $[\text{Fe}/\text{H}] = 0.0$), and scaled to the stellar radius and distance (Wittenmyer & Marshall 2015; van Leeuwen 2007). We colour corrected the AKARI and WISE flux densities assuming blackbody emission from the star. The resulting spectral energy distribution is shown in the left panel of Figure 10. No evidence of significant excess (i.e. $(F_{\text{obs}} - F_{\star})/\sigma_{\text{obs}} > 3$) from the system is observed out to wavelengths $\sim 22 \mu\text{m}$, ruling out the warm, bright disc inferred from McDonald et al. (2012). The previous identification of infrared excess from HD 86950 can be attributed to the AKARI flux density not being colour corrected.

We performed a similar analysis of the available photometric data for HD 222076. We find no evidence for an excess, with the maximum at $9 \mu\text{m}$ and 1.8σ (Figure 10, right panel). McDonald et al. (2012) likewise find no excess in their analysis.

While we find that HD 29399 does not host a planet, we note that McDonald et al. (2012) also identify it as having an excess, with $(L_{\text{dust}}/L_{\text{star}}) \sim 3.6 \times 10^{-3}$. Using the same approach as described above, we show the spectral energy distribution for HD 29399 in Figure 11. Photometry for the targets was compiled from Johnson BV , 2MASS JHK_s (Cutri et al. 2003), WISE All-Sky Survey (Wright et al. 2010), and the Akari IRC All-Sky Survey (Ishihara et al. 2010). We avoided using WISE W1 and W2 photometry due to known saturation issues for bright ($V < 8$) stars. We fit the stellar photospheric emission with the following model atmosphere consistent with the physical parameters given in Table 5: $T_{\text{eff}} = 4800$ K, $\log g = 3.5$, $[\text{Fe}/\text{H}] = 0.0$. Adopting a stellar radius of $3.97 R_{\odot}$ and the distance as given in Table 5, we find an infrared excess at the 3-8 σ level. This can be fitted with a star+dust model using 1500K dust ($\chi_{\nu}^2 = 1.085$). The star is not yet so evolved (nor is its photospheric temperature cool enough) that it would be expected to be surrounded by a dusty envelope, one potential origin of the excess. Likewise, the radial velocities rule out the presence of a cool binary stellar companion. If we adopt a 25% larger stellar radius of $\sim 5 R_{\odot}$, then the excess disappears and would be consistent with the poorly constrained near-infrared photometry for this star. However, assuming we are confident in the derivation of our stellar parameters and that the circumstellar dust origin for the excess holds, such hot dust might therefore be produced by e.g. delivery of comets from an outer, cool debris belt. Additional measurements of the spectral energy distribution at wavelengths $> 30 \mu$ to search for such a debris belt would be of value in this case.

4.2. The giant planet-metallicity relation

¹ <http://exoplanets.org>, accessed 2016 July

Following recent work by [Reffert et al. \(2015\)](#) and [Jones et al. \(2016\)](#), we now examine the results of the PPPS in light of the planet-metallicity relation for evolved hosts as noted by those authors. Overall, our PPPS sample of 164 stars has 11 confirmed planet hosts, comparable to the 10 planet hosts in 166 stars reported by the EXPRESS survey ([Jones et al. 2016](#)). [Reffert et al. \(2015\)](#) reported 15 secure planet hosts (and a further 20 candidates) among 373 giant stars in their Lick Observatory sample. Figure 12 shows the host-star mass versus metallicity [Fe/H] for 164 PPPS stars; the 11 confirmed hosts are shown as red points.

For ease of comparison, we cast our results into the same stellar mass-metallicity bins as used by [Reffert et al. \(2015\)](#). Table 8 shows the PPPS results in these bins; [Jones et al. \(2016\)](#) presented the EXPRESS results in the same format in their Table 3. Our results are broadly consistent; a key difference is that the PPPS sample has very few targets of super-solar metallicity compared to the EXPRESS and Lick surveys. This results in the highest-metallicity bins being sparsely populated and not quite amenable to a full analysis including the dimension of host-star mass (as was performed for the 373-star sample presented in [Reffert et al. 2015](#)).

We next investigate the occurrence rate only as a function of [Fe/H] as shown in Figure 13. For ease of comparison with [Jones et al. \(2016\)](#), we use the same bins as from their Figure 8. The 68.3% binomial confidence intervals are computed after [Wilson \(1927\)](#), which is noted by [Brown et al. \(2001\)](#) as a preferable method for small sample sizes.

Consistent with [Hekker & Meléndez \(2007\)](#), [Reffert et al. \(2015\)](#), and [Jones et al. \(2016\)](#), we also show an increasing planet occurrence rate with stellar metallicity. The two samples, of planet hosts and the parent sample, are shown by the K-S test to be drawn from the same distribution with a K-S probability of $P = 0.708$, i.e. a 70.8% probability that they are from the same underlying distribution.

Our findings of a positive correlation between metallicity and planet occurrence are in contrast to the results of some other evolved star surveys (e.g. [Pasquini et al. 2007](#); [Takeda et al. 2008](#); [Mortier et al. 2013](#)). The disagreement most likely arises from different selection criteria for the samples of evolved stars observed by the various groups. [Mortier et al. \(2013\)](#) pointed out that since most surveys choose a colour cutoff ($B - V \leq 1.0$), the more metal-rich, low-gravity stars are excluded. To illustrate this, Figure 14 plots the distribution of $\log g$ versus [Fe/H] for the targets of four surveys, two of which find a planet-metallicity correlation ([Jones et al. 2016](#); [Wittenmyer et al. 2016d](#)), and two of which do not ([Takeda et al. 2008](#); [Mortier et al. 2013](#)). The surveys which did not find a correlation are shown as red open circles, generally lying at lower [Fe/H] and lower surface gravity than the others. [Mortier et al. \(2013\)](#) showed a similar result in their Figure 6. We also show the differences in (B-V) colours from these four surveys in the right panel of Figure 14. Again, the surveys finding a planet-metallicity correlation tend to sample redder stars with $(B - V) \geq 1.0$.

These results from the PPPS do not yet account for survey incompleteness induced by nonuniform detectability (e.g. [Howard et al. 2010](#); [Wittenmyer et al. 2011a, 2016c](#)). A more comprehensive analysis of the overall survey completeness is the subject of a forthcoming paper.

We gratefully acknowledge the efforts of PPPS guest observers Brad Carter, Hugh Jones, and Simon O’Toole. This research has made use of NASA’s Astrophysics Data System (ADS), and the SIMBAD database, operated at CDS, Strasbourg, France. This research has also made use of the Exoplanet Orbit Database and the Exoplanet Data Explorer at [exoplanets.org](#) ([Wright et al. 2011](#); [Han et al. 2014](#)).

Software: MOOG ([Snedden 1973](#)), Kurucz ATLAS9 ([Castelli & Kurucz 2003](#))

REFERENCES

- Alves, S., Benamati, L., Santos, N. C., et al. 2015, MNRAS, 448, 2749
- Andersen, J. M., & Korhonen, H. 2015, MNRAS, 448, 3053
- Anglada-Escudé, G., & Tuomi, M. 2015, Science, 347, 1080
- Baranne, A., Queloz, D., Mayor, M., et al. 1996, A&AS, 119, 373
- Berdyugina, S. V. 2005, Living Reviews in Solar Physics, 2
- Boisse, I., Bouchy, F., Hébrard, G., et al. 2011, A&A, 528, A4
- Bonsor, A., Kennedy, G. M., Crepp, J. R., et al. 2013, MNRAS, 431, 3025
- Bowler, B. P., Johnson, J. A., Marcy, G. W., et al. 2010, ApJ, 709, 396
- Brown, L.T., Cai, T.T., & DasGupta, A. 2001, Statistical Science, 16, 101
- Butler, R. P., Marcy, G. W., Williams, E., McCarthy, C., Dosanjuh, P., & Vogt, S. S. 1996, PASP, 108, 500
- Castelli, F., Kurucz, R. L. 2003, IAU Symposium, 210, 20
- Corben, P. M., Carter, B. S., Banfield, R. M., & Harvey, G. M. 1972, Monthly Notes of the Astronomical Society of South Africa, 31, 7
- Croll, B., Dalba, P. A., Vanderburg, A., et al. 2015, arXiv:1510.06434
- Cutri, R. M., Skrutskie, M. F., van Dyk, S., et al. 2003, VizieR Online Data Catalog, 2246,
- Davenport, J. 2015, Ph.D. Thesis,
- De Medeiros, J. R., Alves, S., Udry, S., et al. 2014, A&A, 561, A126

- Diego, F., Charalambous, A., Fish, A. C., & Walker, D. D. 1990, *Proc. SPIE*, 1235, 562
- Döllinger, M. P., Hatzes, A. P., Pasquini, L., Guenther, E. W., & Hartmann, M. 2009, *A&A*, 505, 1311
- Dumusque, X., Santos, N. C., Udry, S., Lovis, C., & Bonfils, X. 2011, *A&A*, 527, A82
- Egan, M. P., Price, S. D., Kraemer, K. E., et al. 2003, *VizieR Online Data Catalog*, 5114,
- Faria, J. P., Haywood, R. D., Brewer, B. J., et al. 2016, *A&A*, 588, A31
- Fischer, D. A., & Valenti, J. 2005, *ApJ*, 622, 1102
- Fischer, D. A., Anglada-Escude, G., Arriagada, P., et al. 2016, *PASP*, 128, 066001
- Gonzalez, G. 1997, *MNRAS*, 285, 403
- Han, E., Wang, S. X., Wright, J. T., et al. 2014, *PASP*, 126, 827
- Haywood, R. D., Collier Cameron, A., Unruh, Y. C., et al. 2016, *MNRAS*, 457, 3637
- Hekker, S., & Meléndez, J. 2007, *A&A*, 475, 1003
- Hekker, S., Snellen, I. A. G., Aerts, C., et al. 2008, *A&A*, 480, 215
- Høg, E., Fabricius, C., Makarov, V. V., et al. 2000, *A&A*, 355, L27
- Houk, N., & Cowley, A. P. 1975, *University of Michigan Catalogue of two-dimensional spectral types for the HD stars. Volume I. Declinations -90 to -53*, by Houk, N.; Cowley, A. P. Ann Arbor, MI (USA): Department of Astronomy, University of Michigan, 19 + 452 p.,
- Houk, N., & Smith-Moore, M. 1988, *Michigan Catalogue of Two-dimensional Spectral Types for the HD Stars. Volume 4, Declinations -26 to -12*. N. Houk, M. Smith-Moore. Department of Astronomy, University of Michigan, Ann Arbor, MI 48109-1090, USA. 14+505 pp. Price US 25.00 (USA, Canada), US 28.00 (Foreign) (1988),
- Howard, A. W., Marcy, G. W., Johnson, J. A., et al. 2010, *Science*, 330, 653
- Ishihara, D., Onaka, T., Kataza, H., et al. 2010, *A&A*, 514, A1
- Johnson, J. A., Marcy, G. W., Fischer, D. A., Henry, G. W., Wright, J. T., Isaacson, H., & McCarthy, C. 2006, *ApJ*, 652, 1724
- Johnson, M. C., Endl, M., Cochran, W. D., et al. 2016, *ApJ*, 821, 74
- Jones, M. I., & Jenkins, J. S. 2014, *A&A*, 562, A129
- Jones, M. I., Jenkins, J. S., Rojo, P., & Melo, C. H. F. 2011, *A&A*, 536, A71
- Jones, M. I., Jenkins, J. S., Rojo, P., Melo, C. H. F., & Bluhm, P. 2013, *A&A*, 556, A78
- Jones, M. I., Jenkins, J. S., Bluhm, P., Rojo, P., & Melo, C. H. F. 2014, *A&A*, 566, A113
- Jones, M. I., Jenkins, J. S., Brahm, R., et al. 2016, *A&A*, 590, A38
- Kaufer, A., Stahl, O., Tubbesing, S., et al. 1999, *The Messenger*, 95, 8
- Kochukhov, O., Makaganiuk, V., & Piskunov, N. 2010, *A&A*, 524, A5
- Landolt, A. U. 1983, *AJ*, 88, 853
- Lovis, C., & Mayor, M. 2007, *A&A*, 472, 657
- Maldonado, J., Villaver, E., & Eiroa, C. 2013, *A&A*, 554, A84
- Martínez-Arnáiz, R., Maldonado, J., Montes, D., Eiroa, C., & Montesinos, B. 2010, *A&A*, 520, A79
- McDonald, I., Zijlstra, A. A., & Boyer, M. L. 2012, *MNRAS*, 427, 343
- Meschiari, S., Wolf, A. S., Rivera, E., et al. 2009, *PASP*, 121, 1016
- Mortier, A., Santos, N. C., Sousa, S. G., et al. 2013, *A&A*, 557, A70
- Pasquini, L., Döllinger, M. P., Weiss, A., et al. 2007, *A&A*, 473, 979
- Pojmanski, G., & Maciejewski, G. 2004, *Acta Astronomica*, 54, 153
- Pollack, J. B., Hubickyj, O., Bodenheimer, P., et al. 1996, *Icarus*, 124, 62
- Rajpaul, V., Aigrain, S., & Roberts, S. 2016, *MNRAS*, 456, L6
- Rappaport, S., Gary, B. L., Kaye, T., et al. 2016, *MNRAS*, 458, 3904
- Reffert, S., Bergmann, C., Quirrenbach, A., Trifonov, T., Künstler, A. 2015, *A&A*, 574, A116
- Reiners, A., Bean, J. L., Huber, K. F., et al. 2010, *ApJ*, 710, 432
- Robertson, P., Mahadevan, S., Endl, M., & Roy, A. 2014, *Science*, 345, 440
- Robertson, P., Roy, A., & Mahadevan, S. 2015, *ApJL*, 805, L22
- Rothman, L. S., Gordon, I. E., Babikov, Y., et al. 2013, *JQSRT*, 130, 4
- Santos, N. C., Israelian, G., & Mayor, M. 2001, *A&A*, 373, 1019
- Santos, N. C., Gomes da Silva, J., Lovis, C., & Melo, C. 2010, *A&A*, 511, A54
- Sato, B., Kambe, E., Takeda, Y., et al. 2005, *PASJ*, 57, 97
- Sato, B., Omiya, M., Wittenmyer, R. A., et al. 2013, *ApJ*, 762, 9
- Sato, B., Wang, L., Liu, Y.-J., et al. 2016, *ApJ*, 819, 59
- Skrutskie, M. F., Cutri, R. M., Stiening, R., et al. 2006, *AJ*, 131, 1163
- Snedden, C. 1973, *ApJ*, 184, 839
- Strassmeier, K. G. 2009, *A&A Rv*, 17, 251
- Takeda, Y., Sato, B., & Murata, D. 2008, *PASJ*, 60, 781
- Tinney, C. G., Wittenmyer, R. A., Butler, R. P., et al. 2011, *ApJ*, 732, 31
- van Leeuwen, F. 2007, *A&A*, 474, 653
- Tokovinin, A., Fischer, D. A., Bonati, M., et al. 2013, *PASP*, 125, 1336
- Valenti, J. A., Butler, R. P. & Marcy, G. W. 1995, *PASP*, 107, 966.
- Vanderburg, A., Johnson, J. A., Rappaport, S., et al. 2015, *Nature*, 526, 546
- Wilson, E.B. 1927, *J. Amer. Statist. Assoc.*, 22, 209
- Wittenmyer, R. A., Tinney, C. G., Butler, R. P., et al. 2011a, *ApJ*, 738, 81
- Wittenmyer, R. A., Endl, M., Wang, L., et al. 2011b, *ApJ*, 743, 184
- Wittenmyer, R. A., & Marshall, J. P. 2015, *AJ*, 149, 86
- Wittenmyer, R. A., Wang, L., Liu, F., et al. 2015, *ApJ*, 800, 74
- Wittenmyer, R. A., Butler, R. P., Wang, L., et al. 2016a, *MNRAS*, 455, 1398
- Wittenmyer, R. A., Johnson, J. A., Butler, R. P., et al. 2016b, *ApJ*, 818, 35
- Wittenmyer, R. A., Butler, R. P., Tinney, C. G., et al. 2016c, *ApJ*, 819, 28
- Wittenmyer, R. A., Liu, F., Wang, L., et al. 2016d, *AJ*, 152, 19
- Wright, E. L., Eisenhardt, P. R. M., Mainzer, A. K., et al. 2010, *AJ*, 140, 1868-1881
- Wright, J. T., Fakhouri, O., Marcy, G. W., et al. 2011, *PASP*, 123, 412
- Zechmeister, M., Kürster, M. 2009, *A&A*, 496, 577
- Zieliński, P., Niedzielski, A., Adamów, M., & Wolszczan, A. 2010, *EAS Publications Series*, 42, 201

Table 1. Summary of observations

Star	N_{obs}	Span (days)	Mean uncertainty (m s^{-1})	Instrument
HD 29399	22	2373	1.8	UCLES
	7	79	4.2	CHIRON
HD 86950	13	1879	2.8	UCLES
	7	66	3.9	CHIRON
HD 222076	11	1456	2.5	UCLES
	17	2072	4.3	FEROS
	9	149	7.2	CHIRON

Table 2. Radial velocities for HD 29399

BJD-2400000	Velocity (m s^{-1})	Uncertainty (m s^{-1})	Instrument
54866.93634	-24.01	4.68	AAT
54867.96653	-23.57	1.04	AAT
54869.89726	-15.40	1.32	AAT
54870.90323	-11.30	1.15	AAT
55074.31485	22.61	1.40	AAT
55075.31193	21.45	1.23	AAT
55140.16735	26.33	1.76	AAT
55225.01910	1.75	0.68	AAT
55225.91346	15.36	0.77	AAT
55226.92603	6.46	0.91	AAT
55455.23879	-35.32	4.05	AAT
55525.12752	-31.79	1.00	AAT
55580.91947	-40.68	1.07	AAT
55601.91656	-24.89	1.62	AAT
55783.26560	10.02	2.60	AAT
55879.16028	12.69	1.31	AAT
55906.05799	21.17	1.06	AAT
55971.05135	34.47	1.21	AAT
56344.94543	-23.99	1.32	AAT
56375.87846	-5.35	1.24	AAT
56526.22058	1.91	5.67	AAT
57238.28861	-5.13	1.55	AAT
57298.82760	-6.50	4.30	CHIRON
57299.74140	-8.70	4.80	CHIRON
57308.68060	19.90	4.30	CHIRON
57324.81200	9.20	4.40	CHIRON
57332.68480	2.30	3.90	CHIRON
57353.71510	-6.00	4.20	CHIRON
57377.59490	-10.10	3.80	CHIRON

NOTE—The velocities shown are relative to instrument-specific zero points.

Table 3. Radial velocities for HD 86950

BJD-2400000	Velocity (m s^{-1})	Uncertainty (m s^{-1})	Instrument
54866.15767	28.67	2.43	AAT
55252.08271	-31.39	4.95	AAT
55381.85809	-42.55	1.85	AAT
55581.16782	7.70	1.97	AAT
55969.12369	51.80	2.08	AAT
55994.08537	60.23	3.44	AAT
56051.93221	36.53	5.64	AAT
56090.89459	50.92	2.72	AAT
56344.07002	-7.25	3.33	AAT
56375.04442	-11.47	2.34	AAT
56377.01080	-10.30	1.98	AAT
56399.95118	0.00	1.99	AAT
56745.02214	-19.00	2.18	AAT
57394.72380	3.40	4.10	CHIRON
57404.86600	4.70	3.80	CHIRON
57406.82630	4.90	4.20	CHIRON
57407.85770	-7.40	4.50	CHIRON
57445.62610	5.30	3.70	CHIRON
57445.64010	-0.20	3.20	CHIRON
57460.60950	-10.60	3.80	CHIRON

NOTE—The velocities shown are relative to instrument-specific zero points, which are free parameters in the fitting process and are given in Table 6.

Table 4. Radial velocities for HD 222076

BJD-2400000	Velocity (m s^{-1})	Uncertainty (m s^{-1})	Instrument
55074.25071	-31.5	1.8	AAT
55495.99749	20.2	2.1	AAT
55525.93596	30.4	2.6	AAT
55788.26403	-31.1	3.4	AAT
56052.29321	-0.7	3.7	AAT
56089.28126	1.1	2.3	AAT
56400.31160	22.9	2.0	AAT
56469.30504	1.0	3.2	AAT
56494.25818	-1.9	2.1	AAT
56526.10530	0.0	1.7	AAT
56530.11951	-6.1	2.1	AAT
55317.88970	16.0	4.6	FEROS
55379.90380	31.1	3.6	FEROS
55428.75550	17.6	4.0	FEROS
55457.72790	15.1	3.6	FEROS
55729.91020	-19.6	5.0	FEROS
55786.89910	-39.4	4.6	FEROS
55793.83430	-31.0	4.2	FEROS
56047.93430	-18.7	3.0	FEROS

Table 4 continued on next page

Table 4 (*continued*)

BJD-2400000	Velocity (m s^{-1})	Uncertainty (m s^{-1})	Instrument
56160.79830	7.7	3.3	FEROS
56241.62910	23.0	3.4	FEROS
56251.66450	9.8	3.9	FEROS
56412.86280	10.8	4.1	FEROS
56431.84030	-0.9	3.1	FEROS
56565.68380	-27.2	3.7	FEROS
57174.87230	17.1	3.8	FEROS
57388.55510	-9.8	4.2	FEROS
57389.55090	-1.6	4.0	FEROS
57255.75540	3.9	6.7	CHIRON
57273.74490	11.3	7.4	CHIRON
57293.66430	16.7	6.8	CHIRON
57311.66690	17.5	7.4	CHIRON
57332.57240	-4.3	7.2	CHIRON
57353.53290	-9.7	6.6	CHIRON
57374.53140	-3.0	7.2	CHIRON
57394.53520	-14.0	8.5	CHIRON
57404.54130	-18.5	7.4	CHIRON

NOTE—The velocities shown are relative to instrument-specific zero points, which are free parameters in the fitting process and are given in Table 6.

Table 5. Stellar Parameters

Parameter	HD 29399		HD 86950		HD 222076	
	Value	Ref.	Value	Ref.	Value	Ref.
Spec. Type	K1 III	2	K1 III	8	K0 III	7
$(B - V)$	1.03	9	1.09	10	1.030	8
$E(B - V)$	0.0053	1	0.0173	1	0.0121	1
A_V	0.0165	1	0.0537	1	0.0374	1
Mass (M_\odot)	1.68 ± 0.25	1	1.66 ± 0.25	1	1.07 ± 0.25	1
Distance (pc)	45.1 ± 0.5	4	169 ± 22	4	83.5 ± 4.3	4
$[Fe/H]$	0.07 ± 0.10	1	0.04 ± 0.10	1	0.05 ± 0.10	1
T_{eff} (K)	0.11 ± 0.03	3	0.08 ± 0.09	7	0.16	6
	4848 ± 100	1	4805 ± 100	1	4806 ± 100	1
	4828 ± 53	3	4900	6		
$\log g$	5170	5	4861	5	4950	5
	3.33 ± 0.15	1	2.66 ± 0.15	1	3.31 ± 0.15	1
Luminosity (L_\odot)	3.27 ± 0.16	3	3.18	6		
	10.0	1	36.3	1	8.5	1
Radius (R_\odot)	9.56	5	33.38	5	7.84	5
	4.0 ± 0.6	1	8.8 ± 0.6	1	4.1 ± 0.6	1

NOTE—References: 1 - [Wittenmyer et al. \(2016d\)](#), 2 - [Houk & Cowley \(1975\)](#), 3 - [Alves et al. \(2015\)](#), 4 - [van Leeuwen \(2007\)](#), 5 - [McDonald et al. \(2012\)](#), 6 - [Jones et al. \(2011\)](#), 7 - [Houk & Smith-Moore \(1988\)](#), 8 - [Landolt \(1983\)](#), 9 - [Corben et al. \(1972\)](#), 10 - [Høg et al. \(2000\)](#)

Table 6. Keplerian orbital solutions

Parameter	HD 86950b	HD 222076b
Period (days)	1270 ± 57	871 ± 19
T_0 (BJD-2400000)	54245 ± 161	54264 ± 189
Eccentricity	0.17 ± 0.16	0.08 ± 0.05
ω (degrees)	243 ± 70	241 ± 60
K (m s^{-1})	49 ± 12	31.9 ± 2.3
$m \sin i$ (M_{Jup})	3.6 ± 0.7	1.56 ± 0.11
a (AU)	2.72 ± 0.08	1.83 ± 0.03
RMS about fit (m s^{-1})	6.1	5.9
Zero point – AAT m s^{-1}	13.9 ± 4.7	-1.6 ± 2.1
Zero point – FEROS m s^{-1}	...	-10.3 ± 1.8
Zero point – CHIRON m s^{-1}	-17.8 ± 20.4	-10.3 ± 5.3

Table 7. FEROS activity indicators for HD 222076

BJD-2400000	BVS (m s^{-1})	FWHM (km s^{-1})	S_{MW}
55317.8897	0.6 ± 10.9	12.749 ± 0.065	0.138 ± 0.004
55379.9038	-6.1 ± 7.3	12.767 ± 0.076	0.131 ± 0.002

Table 7 continued on next page

Table 7 (*continued*)

BJD-2400000	BVS (m s^{-1})	FWHM (km s^{-1})	S_{MW}
55428.7555	-20.4±12.4	12.753±0.064	0.125±0.002
55457.7279	-24.1±7.9	12.855±0.077	0.127±0.002
55729.9102	-5.4±8.4	12.854±0.072	0.125±0.003
55786.8991	-12.0±9.8	12.841±0.076	0.134±0.002
55793.8343	-29.2±8.3	12.848±0.075	0.133±0.003
56047.9343	17.2±6.6	12.856±0.077	0.128±0.002
56160.7983	-39.0±9.4	12.835±0.072	0.126±0.002
56241.6291	-22.8±13.6	12.767±0.063	0.131±0.002
56251.6645	1.5±12.7	12.832±0.072	0.117±0.002
56412.8628	-1.0±10.5	12.716±0.067	0.093±0.004
56431.8403	-7.7±7.5	12.793±0.066	0.137±0.004
56565.6838	-10.2±12.4	12.811±0.066	0.122±0.002
57174.8723	-2.7±7.0	12.780±0.068	0.126±0.002
57388.5551	-32.4±11.2	12.825±0.072	0.132±0.002
57389.5509	-20.7±13.6	12.738±0.065	0.125±0.002

NOTE—BVS – bisector velocity span; FWHM – full-width half max of the cross-correlation function; S_{MW} – Mount Wilson S-index.

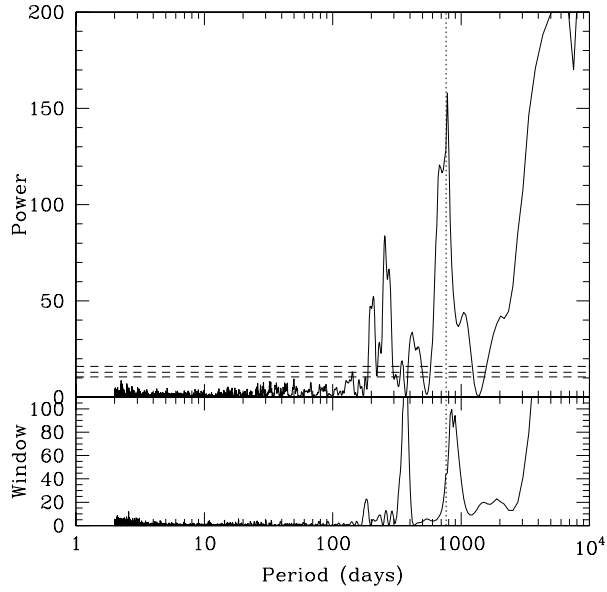


Figure 1. Generalised Lomb-Scargle periodogram of ASAS photometry for HD 29399. A highly significant peak is present at the period of the radial velocity signal (765 days, dotted line). 10%, 1%, and 0.1% bootstrap-derived false alarm probabilities are shown as horizontal dashed lines.

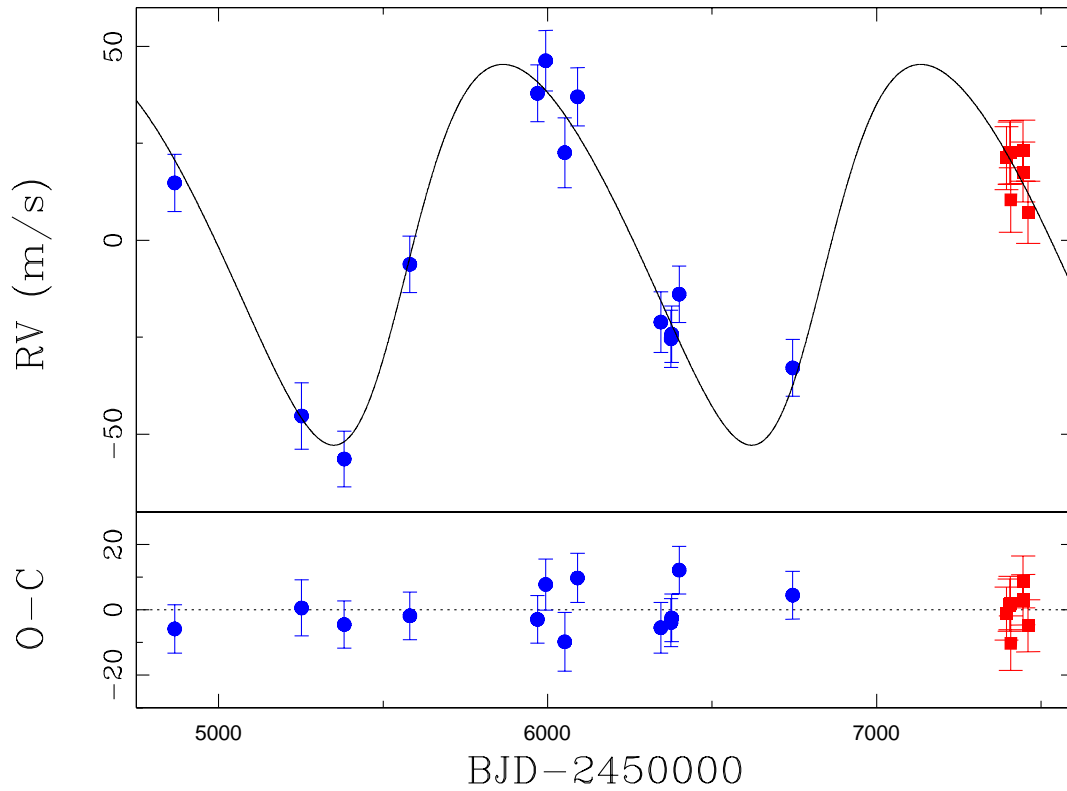


Figure 2. Data and Keplerian fit for a $3.6M_{\text{Jup}}$ planet orbiting HD 86950 (AAT – blue, CHIRON – red). Error bars include 7 m s^{-1} of jitter added in quadrature. The rms about this fit is 6.1 m s^{-1} .

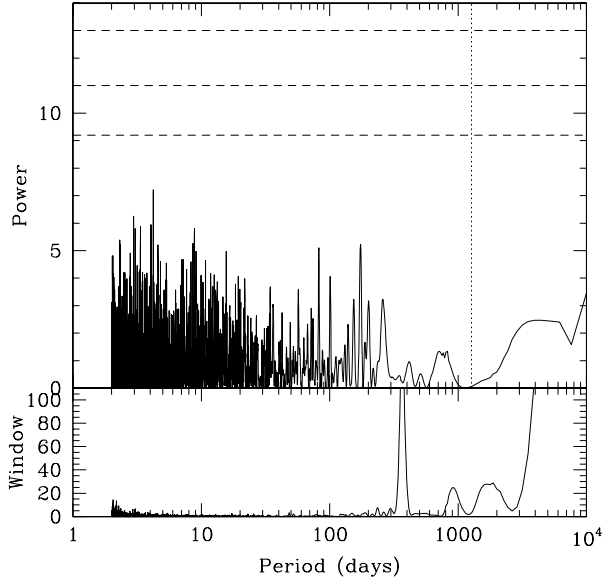


Figure 3. Generalised Lomb-Scargle periodogram of ASAS photometry for HD 86950. A total of 515 epochs spanning 8.9 years yield no significant periodicities. The 1291-day period of the planet is marked with a dotted line. 10%, 1%, and 0.1% bootstrap-derived false alarm probabilities are shown as horizontal dashed lines.

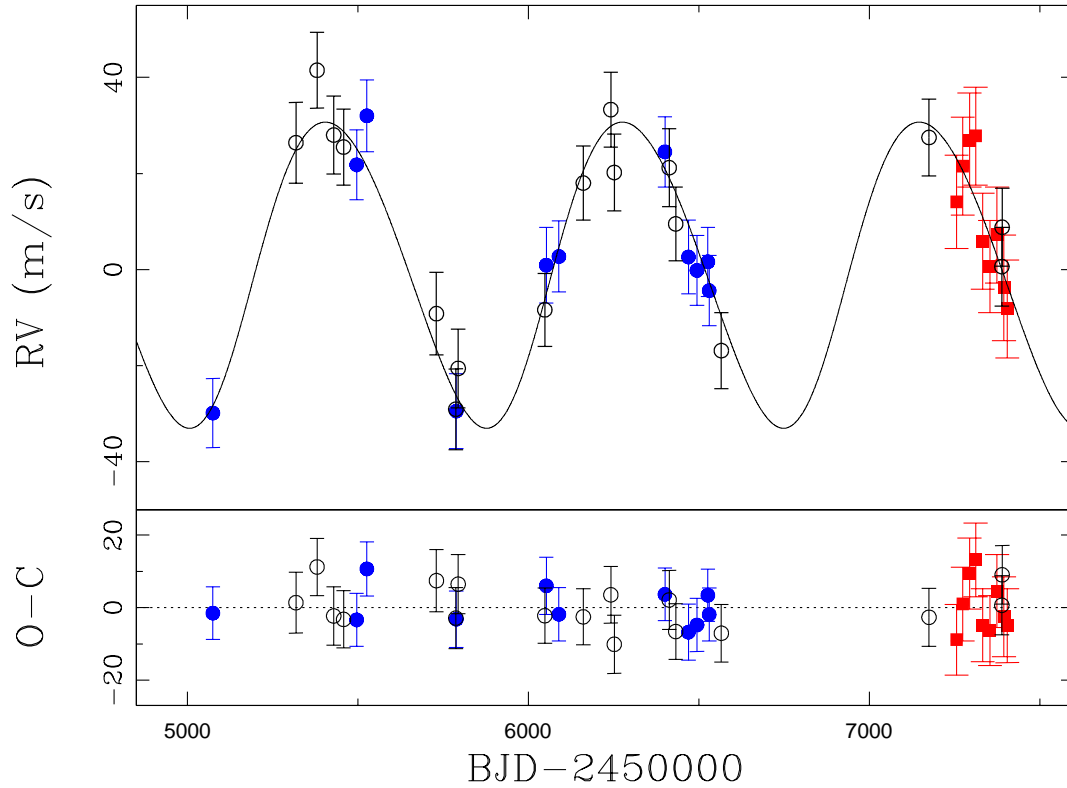


Figure 4. Data and Keplerian fit for a $1.6M_{\text{Jup}}$ planet orbiting HD 222076 (AAT – blue, FEROS – open, CHIRON – red). Error bars include 7 m s^{-1} of jitter added in quadrature. The rms about this fit is 5.9 m s^{-1} .

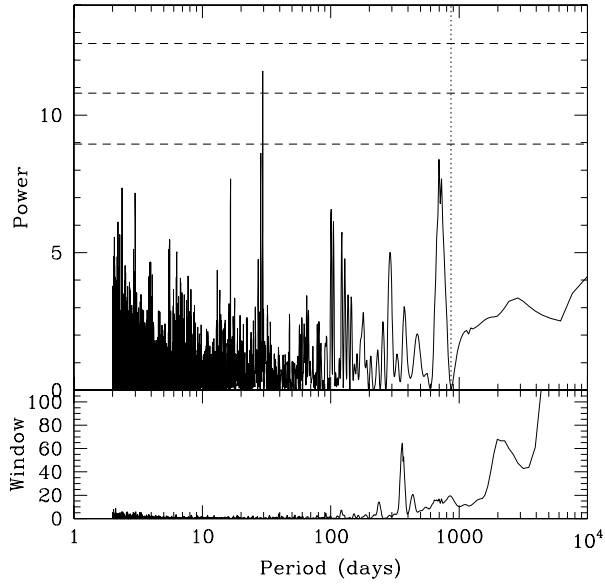


Figure 5. Generalised Lomb-Scargle periodogram of ASAS photometry for HD 222076. A total of 425 epochs spanning 8.8 years yield no significant periodicities. The 868-day period of the planet is marked with a dotted line. 10%, 1%, and 0.1% bootstrap-derived false alarm probabilities are shown as horizontal dashed lines.

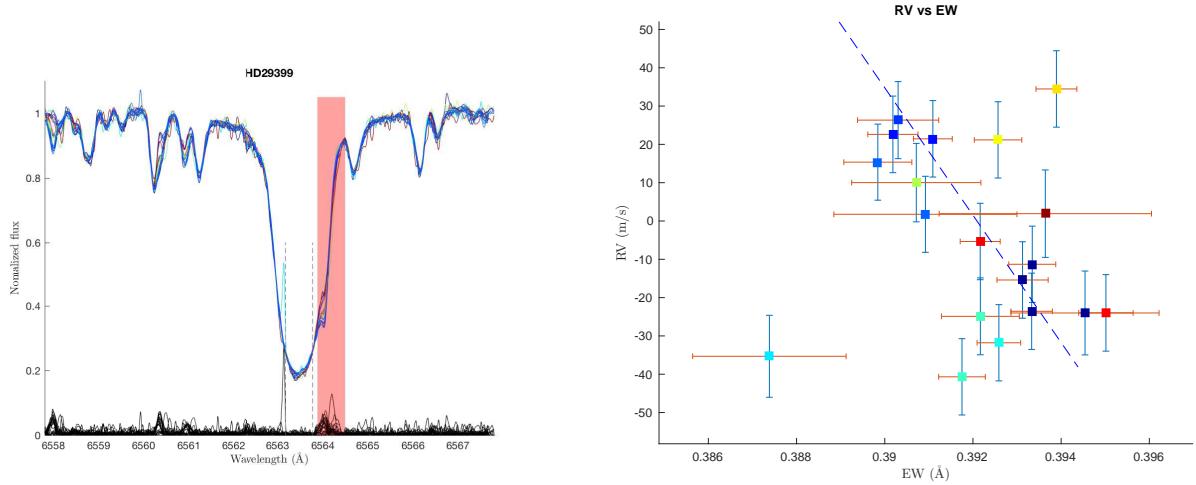


Figure 6. Left: the individual normalized spectra stacked on top of each other. The 0.5 Å H α region is labelled within the black dashed lines, whereas the telluric region is the shaded area within red dashed lines. Differences from the template are shown at the bottom. Large residuals are due to telluric contamination. Right: Radial velocity versus H α equivalent width. The same epoch is presented in identical colours across these two panels, and the closeness in colour within the same panel represents the closeness in BJD.

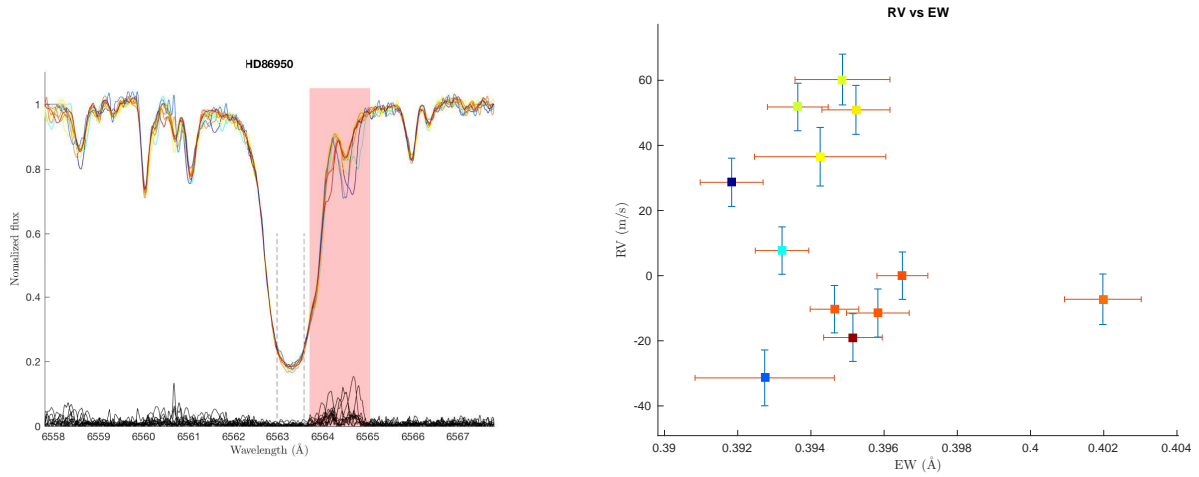


Figure 7. Same as Fig. 7, but for HD 222076.

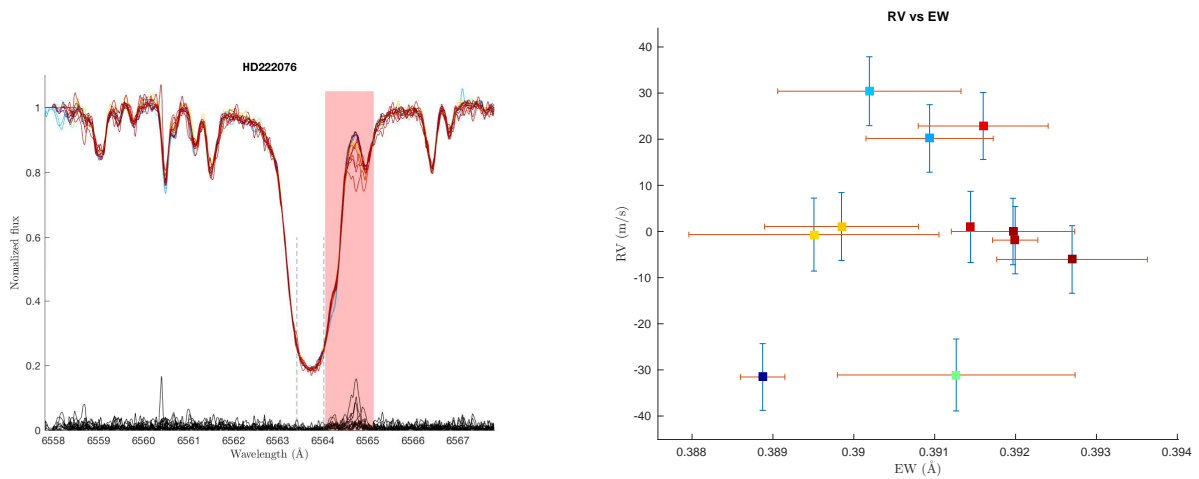


Figure 8. Same as Fig. 7, but for HD 222076.

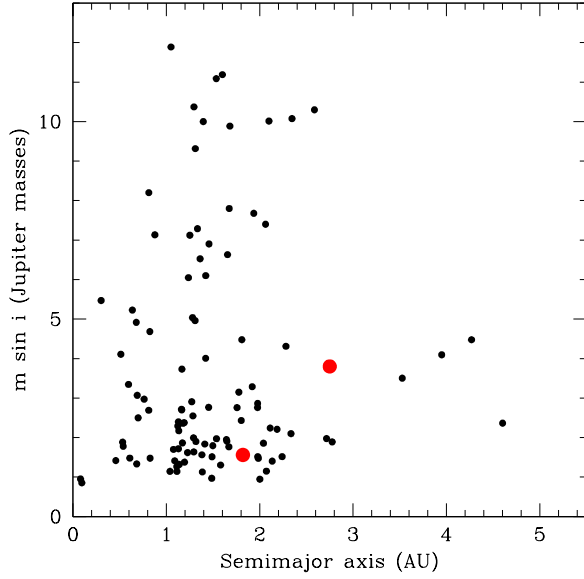


Figure 9. Masses and semimajor axes of 107 planets orbiting giant stars (planet data obtained from the Exoplanet Orbit Database at exoplanets.org). The two larger red points are HD 86950b and HD 222076b. These new planets are entirely typical of the evolved-host population.

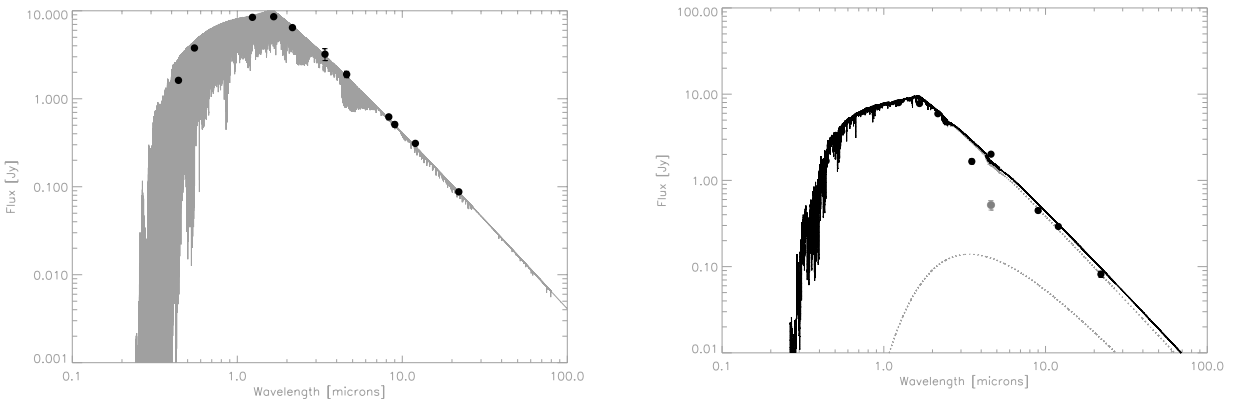


Figure 10. Left: Spectral energy distribution of HD 86950. The photometric data compiled from literature sources are shown in black, with $1\text{-}\sigma$ uncertainties. The stellar photosphere model is shown in grey, and has been scaled according to the assumed stellar radius and parallax-derived distance (i.e. it is not a least-squares fit to the photometry). No evidence of infrared excess at the observed wavelengths is present. Right: Same, but for HD 222076.

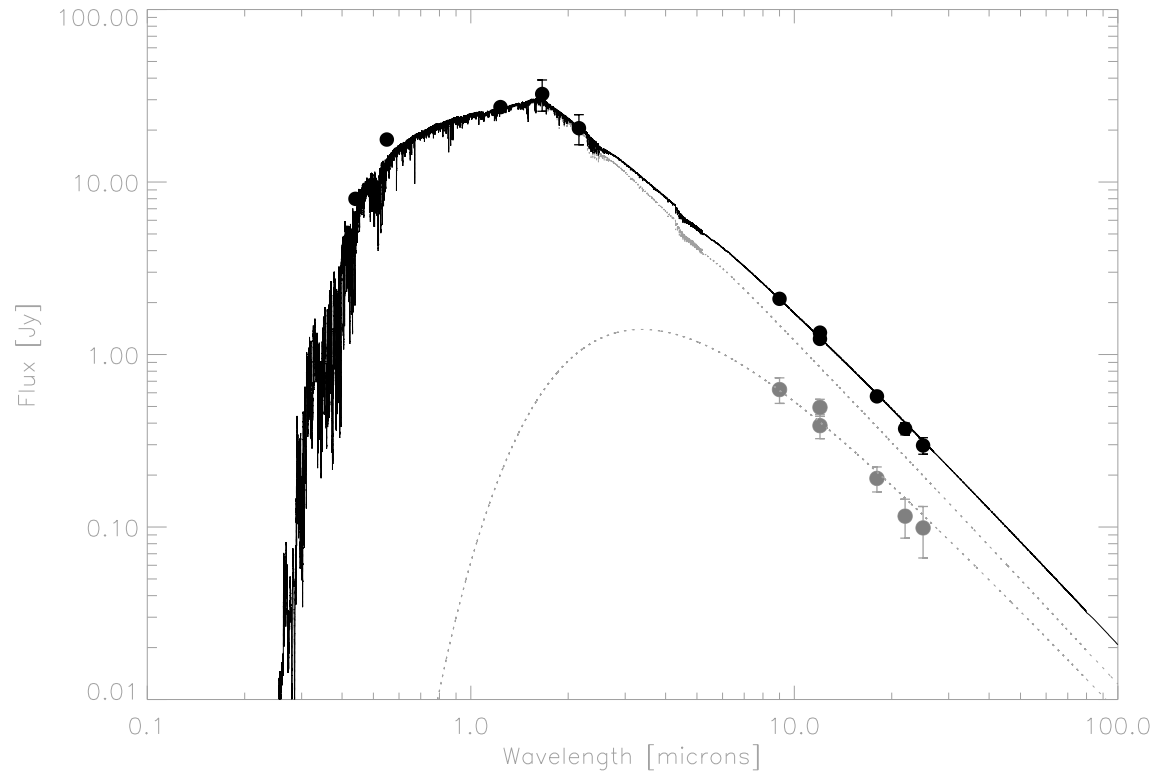


Figure 11. Spectral energy distribution of HD 29399. An excess is evident at the $3\text{-}8\sigma$ level, and can be fitted with a star+dust model using 1500 K dust (lower dotted curve).

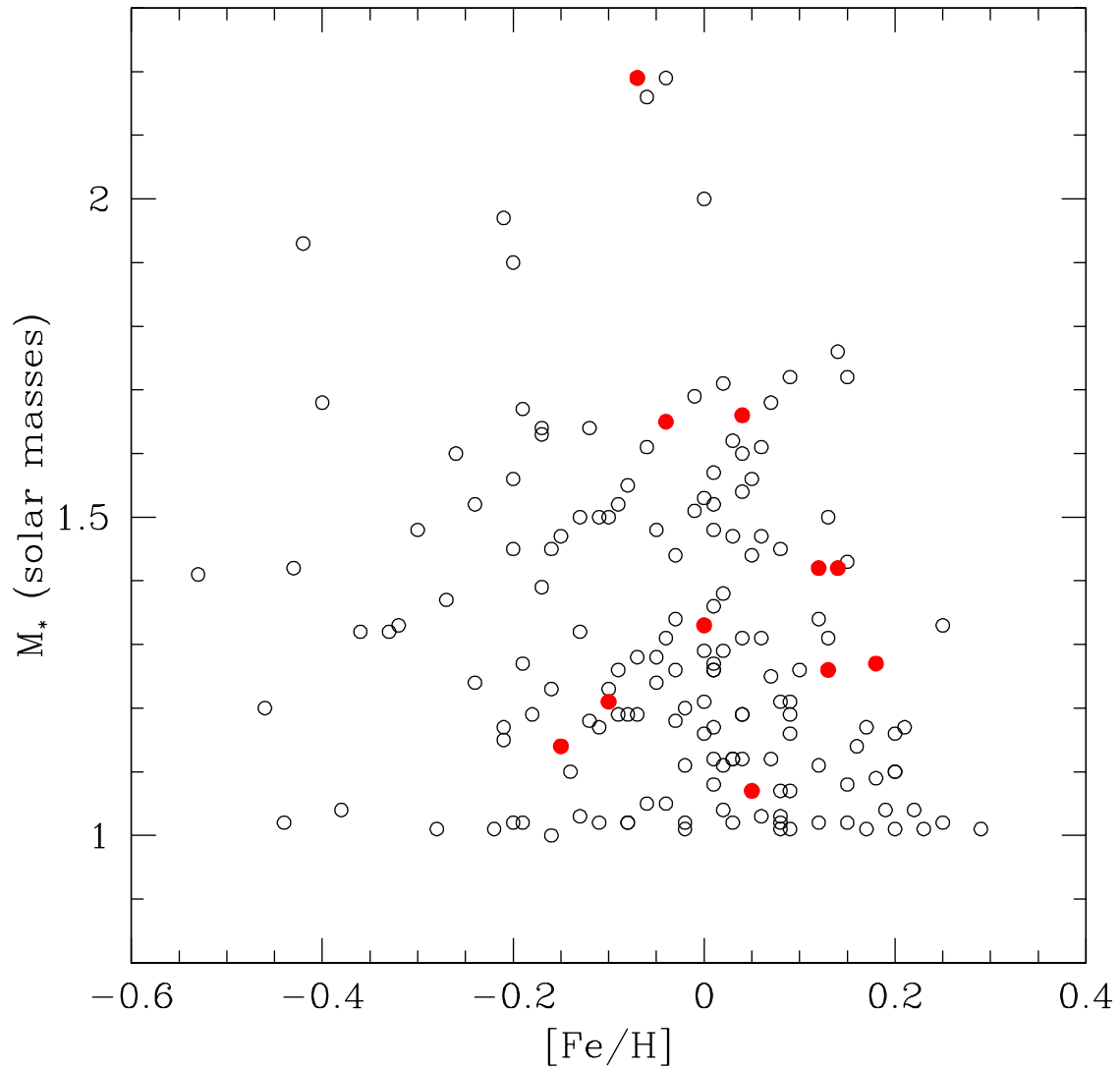


Figure 12. Host-star mass versus metallicity for 164 evolved stars in the PPPS. Stellar parameter data have been taken from [Wittenmyer et al. \(2016d\)](#). Planet hosts are shown as filled red circles.

Table 8. Detection fraction in host star mass/metallicity bins. Bin sizes are the same as in [Reffert et al. \(2015\)](#), their Table 1.

[Fe/H]	M_* (M_\odot)	N_{stars}	N_{hosts}	f (%)
-0.36	1.4	10	0	$0.0^{+9.1}_{-0.0}$
-0.36	2.2	1	0	$0.0^{+50.0}_{-0.0}$
-0.36	3.0	0	0	...
-0.20	1.4	27	1	$3.7^{+5.6}_{-2.3}$
-0.20	2.2	2	0	$0.0^{+33.4}_{-0.0}$
-0.20	3.0	0	0	...
-0.04	1.4	60	4	$6.7^{+4.0}_{-2.6}$

Table 8 continued on next page

Table 8 (*continued*)

[Fe/H]	M_* (M_\odot)	N_{stars}	N_{hosts}	f (%)
-0.04	2.2	4	1	$25.0^{+25.0}_{-15.0}$
-0.04	3.0	0	0	...
+0.12	1.4	49	5	$10.2^{+5.2}_{-3.6}$
+0.12	2.2	0	0	...
+0.12	3.0	0	0	...
+0.28	1.4	10	0	$0.0^{+9.1}_{-0.0}$
+0.28	2.2	0	0	...
+0.28	3.0	0	0	...

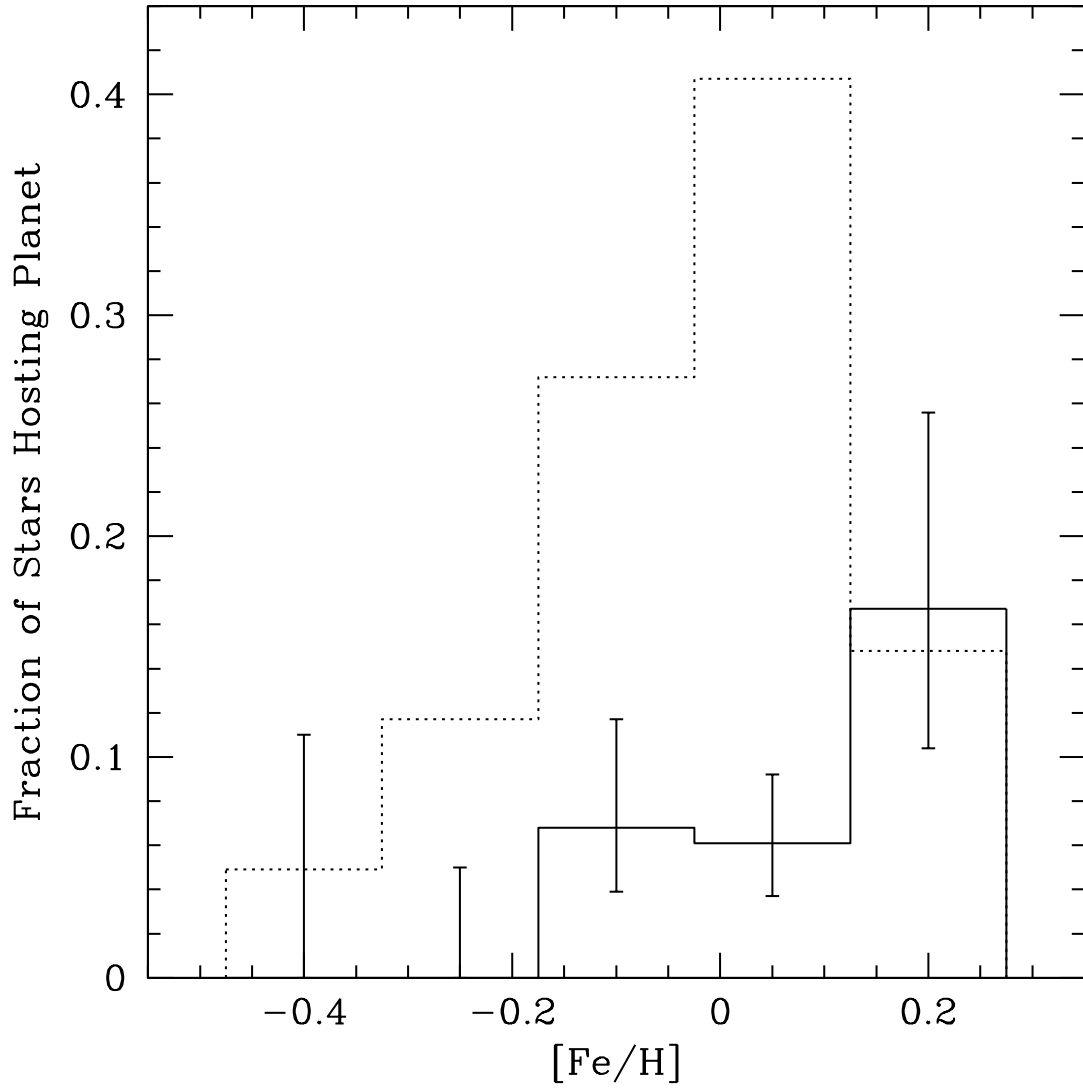


Figure 13. Occurrence rate as a function of metallicity for PPPS targets with confirmed planets. The dashed histogram shows the parent sample distribution. The bins are the same as defined in Figure 8 of [Jones et al. \(2016\)](#).

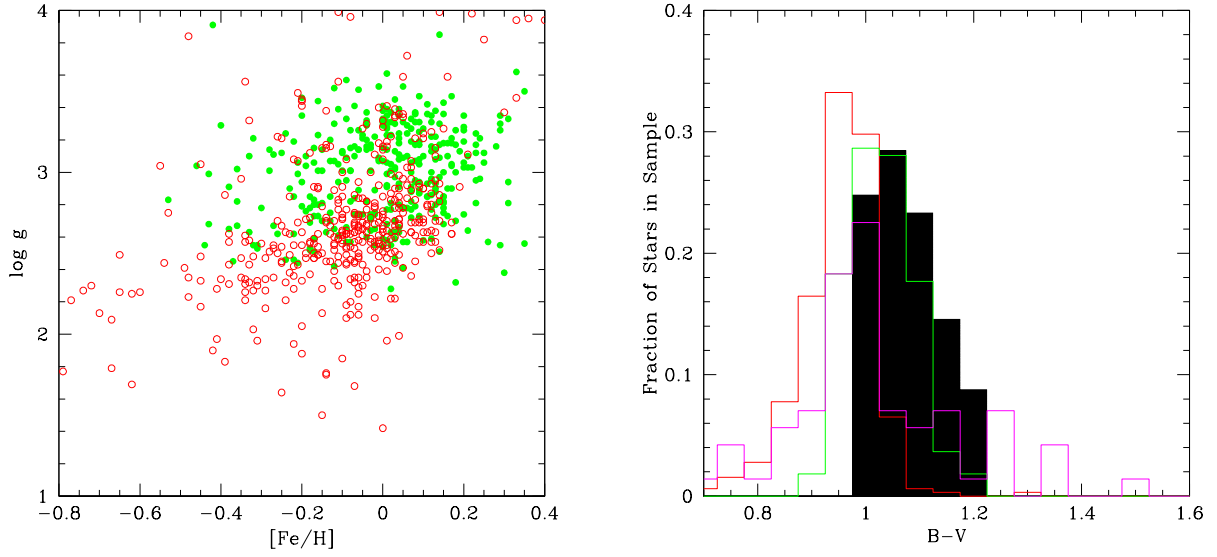


Figure 14. Left: Surface gravity versus $[\text{Fe}/\text{H}]$ for samples of evolved stars for which a planet-metallicity correlation is evident (green filled circles) and not evident (red open circles). The former are drawn from [Jones et al. \(2016\)](#) and [Wittenmyer et al. \(2016d\)](#), while the latter are drawn from [Takeda et al. \(2008\)](#) and [Mortier et al. \(2013\)](#). Right: Normalized distribution of colours of evolved stars from four surveys: solid – [Wittenmyer et al. \(2016d\)](#); green – [Jones et al. \(2016\)](#); red – [Takeda et al. \(2008\)](#); magenta – [Mortier et al. \(2013\)](#). Surveys not finding a planet-metallicity correlation have largely excluded stars redward of $(B - V) = 1.0$, a bias proposed by [Mortier et al. \(2013\)](#) as a possible source of the discrepant conclusions reached by these surveys.

APPENDIX

A. CONTINUUM NORMALIZATION

In our UCLES data, the H α line is recorded in two echelle orders (orders 19 and 20). Our analysis makes use of only the data in order 19. Order 20 (which is closer to the edge of the echellogram format) was found to be more subject to scattered light contamination than order 19, and so delivered systematically poorer normalization. The order 19 spectra were analysed in a 10Å window centred on the H α line.

Our continuum fitting algorithm iteratively masks out pixels in the chosen wavelength range based on (1) their first-derivative (i.e. rejecting pixels until no neighbouring pixel has a gradient slopes larger than 10% of the maximum gradient of the original spectrum section), after which it (2) removes the pixels “left behind” at the bottoms of absorption features by keeping the local maxima and removing the local minima. The remaining unmasked continuum points are then (3) fit with linear regression, which is divided out of the original spectrum S_0 to create a first-pass normalized spectrum s_0 . Cosmic rays are removed from this first-pass continuum-normalised spectrum by rejecting pixels more than 10% above the normalised continuum (i.e. with values $s_0 > 1.1$). Steps (1)-(3) are then repeated using the original spectrum S_0 but with the cosmic ray pixels (i.e. the outliers above the continuum) removed to produce a final continuum-normalized spectrum s_1 .

We then construct a high S/N H α template and with it we remove further cosmic rays from the H α window (labelled within dashed lines in the stacked spectra) by identifying groups of pixels displaying anomalous variability between exposures. We select the normalized spectrum with the highest S/N as a first template T_1 , then shift all other spectra to match the velocity of T_1 , using the velocities of §2, to create a high S/N template T_2 as the weighted average of the individual spectra. We reject pixels in the H α window of individual spectrum that combine to form T_2 which deviate from the normalized mean by more than empirically 21 times the expected noise to signal ratio.

The measurement of H α activity indices can be impacted by the presence of telluric absorption lines. Unfortunately, B star observations of each night are not available for telluric correction. We therefore generate a list of telluric line locations using the HITRAN (High-resolution TRANsmission molecular absorption) database (Rothman et al. 2013), and use this to mask out the regions potentially contaminated by H $_2$ O absorption. In the specific case of our data the prominent line is 6564.258Å at rest frame. The telluric contamination is labelled in the shaded region of the stacked profile.

To avoid the telluric contamination, we define our H α equivalent width as the sum of the normalised flux obtained from above at a 0.5Å window centred at H α line $\sum_{|\lambda - \lambda_{H\alpha}| < 0.5\text{Å}} (1 - F_\lambda)$.